Design method and performance prediction for radial-inflow turbines of high-temperature mini-organic rankine cycle power systems

de Servi, Carlo M.; Burigana, Matteo; Pini, Matteo; Colonna, Piero

DOI
10.1115/1.4043973

Publication date
2019

Document Version
Final published version

Published in
Journal of Engineering for Gas Turbines and Power

Citation (APA)
de Servi, C. M., Burigana, M., Pini, M., & Colonna, P. (2019). Design method and performance prediction for radial-inflow turbines of high-temperature mini-organic rankine cycle power systems. *Journal of Engineering for Gas Turbines and Power*, *141*(9), Article 091021. https://doi.org/10.1115/1.4043973

Design Method and Performance Prediction for Radial-Inflow Turbines of High-Temperature Mini-Organic Rankine Cycle Power Systems

Carlo M. De Servi[1]
Flemish Institute for Technology Research (VITO),
Mol 2400, Belgium
e-mail: carlo.deservi@vito.be

Matteo Burigana
Aerospace Engineering Faculty,
Propulsion and Power Aerospace Engineering,
Delft University of Technology,
Delft 2629 HS, The Netherlands
e-mail: matteo@burigana.it

Matteo Pini
Aerospace Engineering Faculty,
Propulsion and Power Aerospace Engineering,
Delft University of Technology,
Delft 2629 HS, The Netherlands
e-mail: M.Pini@tudelft.nl

Piero Colonna
Professor
Aerospace Engineering Faculty,
Propulsion and Power Aerospace Engineering,
Delft University of Technology,
Delft 2629 HS, The Netherlands
e-mail: P.Colonna@tudelft.nl

The realization of commercial mini organic Rankine cycle (ORC) power systems (tens of kW of power output) is currently pursued by means of various research and development activities. The application driving most of the efforts is the waste heat recovery from long-haul truck engines. Obtaining an efficient mini radial inflow turbine, arguably the most suitable type of expander for this application, is particularly challenging, given the small mass flow rate, and the occurrence of nonideal compressible fluid dynamic effects in the stator. Available design methods are currently based on guidelines and loss models developed mainly for turbochargers. The preliminary geometry is subsequently adapted by means of computational fluid-dynamic calculations with codes that are not validated in case of nonideal compressible flows of organic fluids. An experimental 10 kW mini-ORC radial inflow turbine will be realized and tested in the Propulsion and Power Laboratory of the Delft University of Technology, with the aim of providing measurement datasets for the validation of computational fluid dynamics (CFD) tools and the calibration of empirical loss models. The fluid dynamic design and characterization of this machine is reported here. Notably, the turbine is designed using a meanline model in which fluid-dynamic losses are estimated using semi-empirical correlations for conventional radial turbines. The resulting impeller geometry is then optimized using steady-state three-dimensional computational fluid dynamic models and surrogate-based optimization. Finally, a loss breakdown is performed and the results are compared against those obtained by three-dimensional unsteady fluid-dynamic calculations. The outcomes of the study indicate that the optimal layout of mini-ORC turbines significantly differs from that of radial-inflow turbines (RIT) utilized in more traditional applications, confirming the need for experimental campaigns to support the conception of new design practices. [DOI: 10.1115/1.4043973]

1 Introduction

The development of low-capacity high-temperature organic Rankine cycle (ORC) power systems is increasingly pursued, because the creation of large markets for distributed renewable energy conversion and mobile/stationary heat recovery is deemed possible [1]. To achieve high conversion efficiency, the system expander must be a turbine because of the limitation on the maximum pressure ratio affecting rotary volumetric machines. The radial-inflow turbine (RIT) configuration is arguably the best, due to the assembly compactness, high power density, and capability of operating with high flow coefficient at rotor outlet. On the other hand, achieving high expansion efficiency is particularly challenging: the combined effect of high-pressure ratio (order of 30–50) and low speed of sound characteristic of organic vapors used in high-temperature ORC applications [2] leads to the design of machines with a supersonic radial stator and a transonic mixed-flow rotor, whose design is further complicated by their small dimensions. It follows that the design rules developed for more conventional radial turbines [3–5] are arguably inapplicable to this type of expanders, as opposed to mini-ORC radial inflow turbines for low-enthalpy applications [6] or those designed for larger power capacity, which feature moderate expansion ratios, in general not exceeding 12 [7–9].

Recent work related to high-temperature mini-ORC radial-inflow turbines focused on the design and performance prediction of the supersonic radial vanes [10,11] using numerical methods. In Ref. [12], the authors designed small capacity ORC turbines operating with Toluene using only meanline design tools. A thorough study on the detailed design and performance analysis of high-T mini-ORC RIT is not available yet. In addition, for this type of expanders, the establishment of dedicated design guidelines can be obtained only by systematic application of experimentally validated methods and tools, which is presently lacking.

In order to contribute to the bridging of this knowledge gap, a high-speed (~100 krpm) mini-ORC radial-inflow turbine operating with siloxane MM as working fluid will be constructed and tested in the Organic Rankine Cycle Hybrid Integrated Device (ORCHID) [13] of the Propulsion and Power Laboratory of Delft University of Technology. The main aim is to measure the fluid-dynamic performance of mini-ORC expanders under a wide range of operating conditions, and to generate sets of experimental data for (i) the validation of computational fluid dynamics (CFD) tools; (ii) the validation of CFD-based design methodologies; and (iii) the calibration of loss correlations to enhance the reliability of preliminary design methods. These validated tools can subsequently be used to define design practices specifically applicable to high-temperature mini-ORC turbines.

The design process and the resulting layout of the 10 kW mini-ORC turbine are documented, together with a thorough study on its estimated fluid-dynamic performance based on three-dimensional unsteady Reynolds-averaged Navier–Stokes

[1]Corresponding author.

Manuscript received July 9, 2018; final manuscript received June 6, 2019; published online August 2, 2019. Assoc. Editor: David Sánchez.

Table 1 Main characteristics of the mini-ORC turbine resulting from the meanline design

η_{ts}	83%	α_1	78 deg	M_{u-2}	1.8
$\dot{W}$	12 kW	α_2	15 deg	D_2	51.5 mm
ω	98 krpm	β_1	35.5 deg	D_3	28.7 mm
$p_{t,0}$	1810 kPa	β_2	−57.6 deg	b_2	2.0 mm
$T_{t,0}$	573 K	M_1	1.9	b_3	12.3 mm
p_3	44.3 kPa	M_{rel-2}	0.5	ϵ_r	0.1 mm
VR	48	M_{rel-3}	0.9	ϵ_x	0.1 mm

simulations. This work benefits from the preliminary investigation of the authors reported in Ref. [14]. The CFD results allow to evaluate the loss breakdown, thus enabling insights into the main loss mechanisms affecting high-temperature mini-ORC radial-inflow turbines. The off-design fluid-dynamic performance of the designed machine is also predicted in order to assess the feasibility of adopting a single stage supersonic turbine in applications in which part-load operation is relevant. Furthermore, an additional CFD study evaluates the effect of blade solidity on expander efficiency. These results are instrumental to determine the validity of existing correlations for the estimation of the optimal blade number, when applied to this type of turbines.

2 Radial-Inflow Turbine Layout

The first step of the design process is the selection of the configuration (axial, radial-inflow, radial-outflow). This selection is usually performed by means of statistical diagrams like, e.g., the Balje's charts, which relate the machine efficiency to the specific speed N_s and specific diameter D_s. In case of high-temperature mini-ORC turbines, the use of such diagrams is questionable and may lead to erroneous choices, because they were developed for flow machines [15] operating with conventional gases and subsonic/transonic flows. Performance maps for ORC turbines have been recently presented by Da Lio et al. [16,17]. However, these charts do not account for volumetric flow ratios higher than 15, a value which is largely exceeded in high temperature ORC applications where expansion ratios are in the order of 50–70.

In light of the above considerations, the choice of the turbine configuration must rely on more sophisticated methodologies, which are able to take into account nonideal and compressible flow effects. Recent work [18] outlined that, for low-capacity ORC systems with power output of the order of 10 kW, the radial-inflow turbine architecture is possibly the most appropriate, given its ability to handle the high volumetric flow ratio with just a single stage and with reduced rotor tip leakage losses if compared to axial and radial-outflow configurations. For this reason, the first expander to be tested in the ORCHID facility will be a radial-inflow turbine.

2.1 Meanline Design. The meanline design of the turbine has been accomplished with the integrated design methodology described in Ref. [18], whereby the optimal preliminary fluid dynamic design of the turbine and of the thermodynamic cycle is performed simultaneously. The main characteristics of the resulting meanline turbo-expander design with MM as working fluid are summarized in Table 1, while a schematic view of the meridional section of the turbine and the thermodynamic cycle of the ORC system in the $T-s$ diagram are shown in Fig. 1. Notice that the clearance gaps in the rotor have been assumed equal to 0.1 mm. The feasibility of such small tip gaps has been proven by the industrial partner of the project [19].

The total-to-static efficiency of the expander has been predicted by means of the empirical loss model documented in Ref. [20], complemented by a physically based model for the estimation of the mixing losses between the exit section of the supersonic vane and the downstream gap [21]. This model has been developed starting from the balance equations (1)–(3) for the control volume shown in Fig. 2. The model accounts for the fluid-dynamic losses due to shock-waves, and those due to shock-wave mixing with the bulk flow. These quantities are not considered in existing loss models for radial-inflow turbines. The optimal solution features a back-swept rotor configuration, allowing to minimize the incidence losses at the inlet section. The turbine total-to-static efficiency estimated by the mean-line model exceeds 83%.

$$V_1\,\rho_1\,s\,\cos(\alpha_a-\Delta\alpha)=V_a\,\rho_a\,a \tag{1}$$

$$V_a\,\rho_a\,a\,V_1\,\cos(\Delta\alpha)+p_1\,a=\rho_a\,a\,V_a^2+p_a\,a \tag{2}$$

$$h_{t,1}=h_{t,a} \tag{3}$$

2.2 Blading Design. The design of the blades requires overcoming specific challenges: the stator is highly supersonic and the

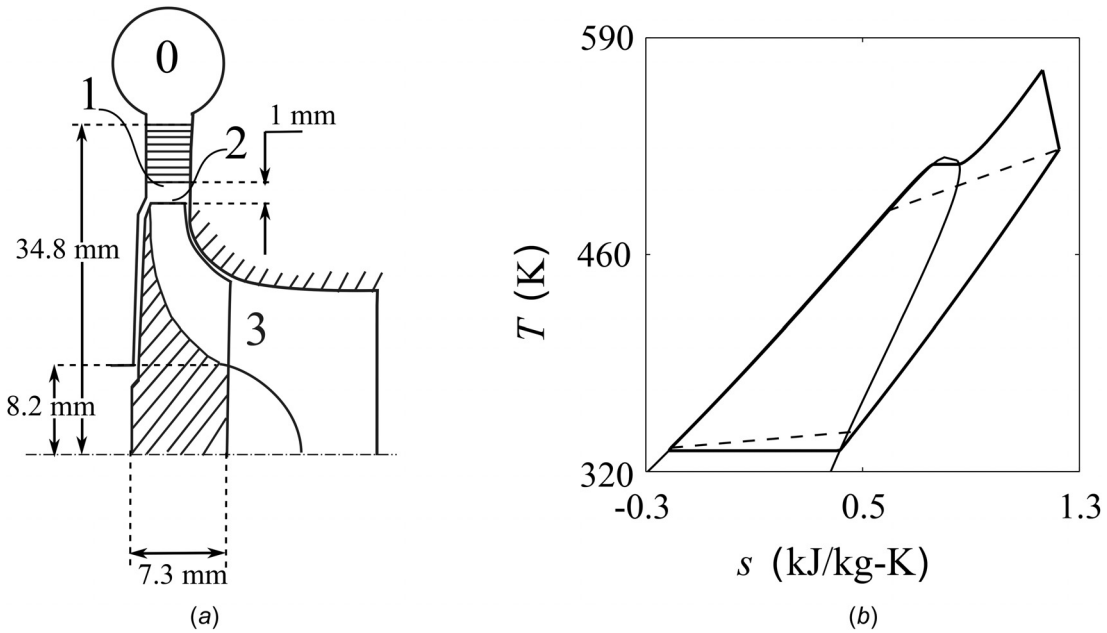

(a) (b)

Fig. 1 (*a*) Meridional section and (*b*) thermodynamic cycle of the ORC system in the *T–s* diagram of MM

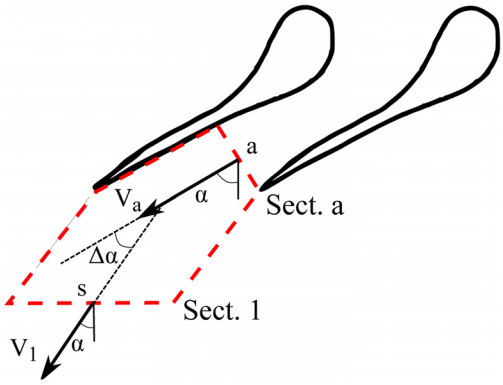

Fig. 2 Control volume considered in the mixing loss model

Table 2 Input values required by the design methodology

Fluid	$p_{t,0}$	$T_{t,0}$	$M_{a,is}$	α_1	N_b	r_0	r_1	t_{te}
MM	1810 kPa	573 K	2.0	78 deg	12	34.8 mm	26.8 mm	0.1 mm

profile of the diverging part of the nozzle, as well as that of rear suction side, is crucial to avoid the onset of strong shock waves [22]. In addition, the flow in the rotor is transonic and flow deflections exceed 90 deg, resulting in comparatively large over-speed on the blade suction side that may eventually trigger flow separation. As a consequence, the vane and rotor blade shapes can be designed only by resorting to specialized design methods.

Notably, the diverging portion of the stator has been designed using the method of characteristics (MoC) for nonideal flows adapted to radial vanes. The prescribed Mach number at the outlet section of the diverging channel, needed to obtain the channel profile with the MoC, has been determined by using the rule proposed in Ref. [23], which provides the optimal area ratio of the diverging part to minimize fluid-dynamic losses arising from viscous and post-expansion effects. The full explanation of the method can be found in Ref. [10]. The main characteristics of the stator vane are reported in Table 2.

As far as the rotor is concerned, a first tentative endwall contour of the impeller has been obtained by following the design guidelines provided in Ref. [24], which suggests a 90 deg circular arc for the shroud and a 90 deg elliptic arc for the hub. Conversely, the camberline curvature has been constructed by assuming a linear variation of the blade metal angle along the meridional length, between the inlet and the outlet values.

These design guidelines, however, have been developed for gas radial turbines with much lower expansion ratios than those characteristic of mini-ORC turbines. The baseline turbine geometry has been, then, refined by means of shape optimization, as shown in the following.

2.2.1 Numerical Model. The fluid-dynamic performance of the turbine has been assessed by means of three-dimensional steady-state CFD simulations performed with a commercial flow solver [25]. The accuracy of the numerical model for mini-ORC radial turbines is not known yet. However, preliminary assessments performed at industrial level on a small capacity radial ORC turbo-expander showed that the CFD model using first-order numerical schemes provides efficiency trends in agreement with those obtained experimentally, see Fig. 3 [19]. Validation with second-order numerical schemes was not achieved due to convergence issues caused by flow separation at the blunt leading-edge of the rotor. Nonetheless, the results prove that the predictive capability of the CFD model is adequate for design purposes. Table 3 reports the used boundary conditions.

The thermo-physical properties of siloxane MM are obtained from look-up tables, according to a procedure provided by the CFD software. Figure 4(*a*) shows the results of a thermodynamic model independence study with the turbine isentropic efficiency as figure of merit. The chosen number of table elements is 500×500. The thermodynamic property values are calculated with a Span-Wagner model [2], while transport property values with the Chung model [26]. Both models are available in another code [27], which has been used to generate the tables.

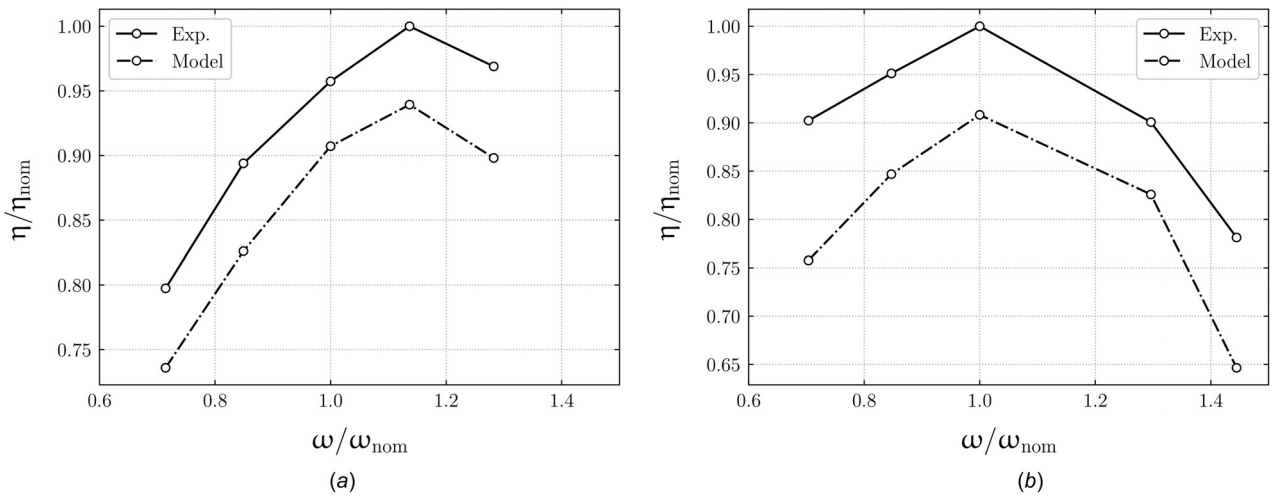

Fig. 3 Efficiency trend of a small capacity ORC radial turbine as a function of the rotational speed for two different expansion ratios, obtained experimentally and by using CFD [19]

Table 3 CFD boundary conditions

$T_{t,0}$ (K)	$p_{t,0}$ (kPa)	Inlet flow direction	Inlet turbulence intensity	p_3 (kPa)	ω (krpm)	Interface
573	1810	⊥ to boundary	5 %	44.3	98.1	Mixing plane

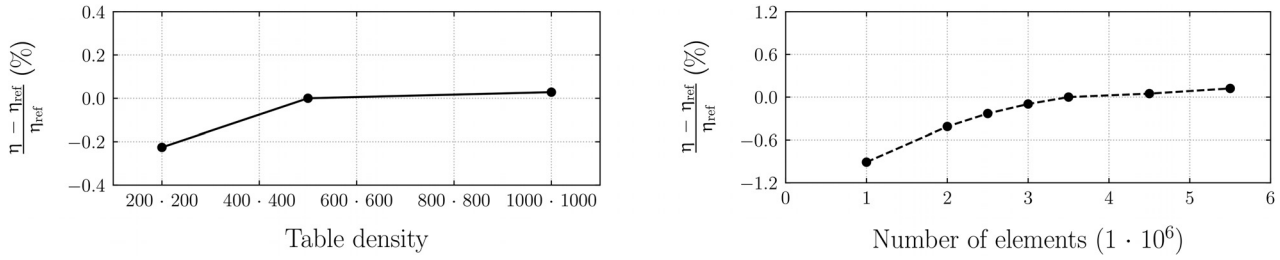

Fig. 4 Results of the grid and look up table independence study shown in terms of normalized total-to-static efficiency: (*a*) look up table and (*b*) grid. η_{ref} indicates the efficiency value estimated with the grid and look up table chosen for CFD computations. The difference between η_{ref} and the efficiency value obtained for the grid and look up table with the highest number of elements is at the most 0.1%.

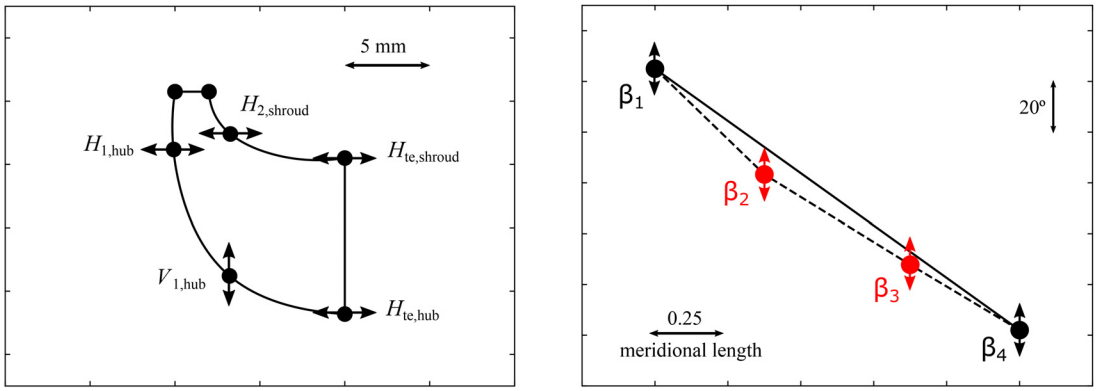

Fig. 5 Rotor parametrization. The arrows show the degree-of-freedom direction: (*a*) meridional channel and (*b*) blade metal angle.

Table 4 Design variables used for the rotor blade optimization. Upper and lower limits are expressed with respect to the starting geometry design values.

	I step: meridional channel	II step: blade to blade channel	III step: flow deflection
1	$-0.4 \le H_{1,hub} \le +0.6$ (mm)	$-75 \le \beta_{2,hub} \le +65$ (deg)	$-40 \le \beta_1 \le +15$ (deg)
2	$-3.5 \le V_{1,hub} \le +6.0$ (mm)	$-60 \le \beta_{3,hub} \le +90$ (deg)	$-10 \le \beta_{4,hub} \le +15$ (deg)
3	$-2.0 \le H_{te,hub} \le +4.0$ (mm)	$-75 \le \beta_{2,shroud} \le +65$ (deg)	$-10 \le \beta_{4,shroud} \le +15$ (deg)
4	$-2.0 \le H_{te,shroud} \le +4.0$ (mm)	$-60 \le \beta_{3,shroud} \le +90$ (deg)	$9 \le N_b \le 27$
5	$-1.0 \le H_{2,shroud} \le +2.0$ (mm)		

The mesh cells of the flow channel have been clustered such that $y^+ < 1$ along the blade surface and $y^+ < 5$ on the endwalls. A grid independence study was carried out and showed that a mesh size of 3.5×10^6 elements is the most suitable in this case, see Fig. 4(*b*). Turbulence effects have been modeled with the k–ω SST closure equations. All the calculations have been run with a second-order spatial discretization scheme for the advective and turbulent fluxes.

2.2.2 Optimization of the Rotor Geometry. The first step to implement shape optimization is to parametrize the impeller geometry. Notably, the meridional channel geometry, the hub and shroud camberlines are parametrized by means of third-order Bezier curves following the method proposed in Ref. [28]. The control points with the corresponding degrees-of-freedom are indicated in Fig. 5.

The optimization is carried out using a surrogate-based optimization algorithm. The chosen objective function is the maximum of the turbine total-to-static efficiency. The set of rotor geometries needed to build the surrogate function is constructed using the Latin hypercube sampling. The range of variation for each design variables is provided in Table 4.

Two different surrogate models, Kriging and nonlinear parametric regression, have been compared in terms of accuracy, defined as the L^2-norm of the deviations between the original CFD model and the reduced-order one. For the problem at hand, the nonlinear parametric regression turned out to be more accurate. Adaptive refinement is used to increase the accuracy of the response surface. Preliminary calculations revealed that the accuracy of the response surface considerably deteriorates when the meridional channel shape and camberline profile are considered simultaneously in the design process. Therefore, the optimization problem has been divided into three sequential design steps, each of them requiring a dedicated surrogate model:

(1) optimization of the hub and shroud of the meridional channel (the five design variables of Fig. 5(*a*));
(2) optimization of the camberline profile at hub and shroud (four degree-of-freedom, see Table 4);
(3) optimization of the rotor solidity, i.e., blade count, and spanwise angle distribution (four design variables).

Table 5 Main turbine design and performance parameters; $\psi = (\Delta h_{tt}/U_2^2)$, $\phi = (V_{m_3}/U_2)$, $R = (\Delta h_{rot}/\Delta h_{tt})$

	Baseline rotor geometry	Optimized rotor geometry
$\dot{m}$ (kg/s)	0.132	0.132
$\dot{W}$ (kW)	10.3	10.6
η_{ts} (%)	81.6	84.0
N_{b-rot}	15	19
$\beta_1 - \beta_2$ (deg)	93.6	98.6
ψ	1.09	1.1
ϕ	0.29	0.29
R	0.35	0.37

The total number of design variables is 13. In the second optimization step, the second and third control points of the rotor camberline in Fig. 5(*b*) have been considered, while in the third step the position of the first and last control point of the camberline is varied. The three response surfaces have been constructed by using 55, 44, and 44 design samples, respectively. For the three optimization problems, the optimal solution is determined by using a hybrid method, consisting of a random search followed by a gradient-based optimization.

The blade shape optimization has led to a total-to-static efficiency gain of about 2.4% with respect to the base case. The main features of the baseline and optimal turbine configurations are summarized in Table 5. Figure 6 shows the flow field at midspan in terms of Mach number and normalized enthalpy loss, defined as $(h - h_{is}/h_{t,0} - h_{3is})$, for both the baseline and optimized turbine geometries. The flow in the channel of the optimized geometry does not display the separation region predicted on the suction side of the rotor blade of the baseline configuration. This results in a reduction of losses along the impeller shroud. The largest fluid-dynamic loss in radial impellers occurs along the shroud due to the convection of low momentum flow toward the tip by the spanwise pressure gradient induced by the meridional channel curvature and the radial component of the Coriolis force, as explained in Ref. [29].

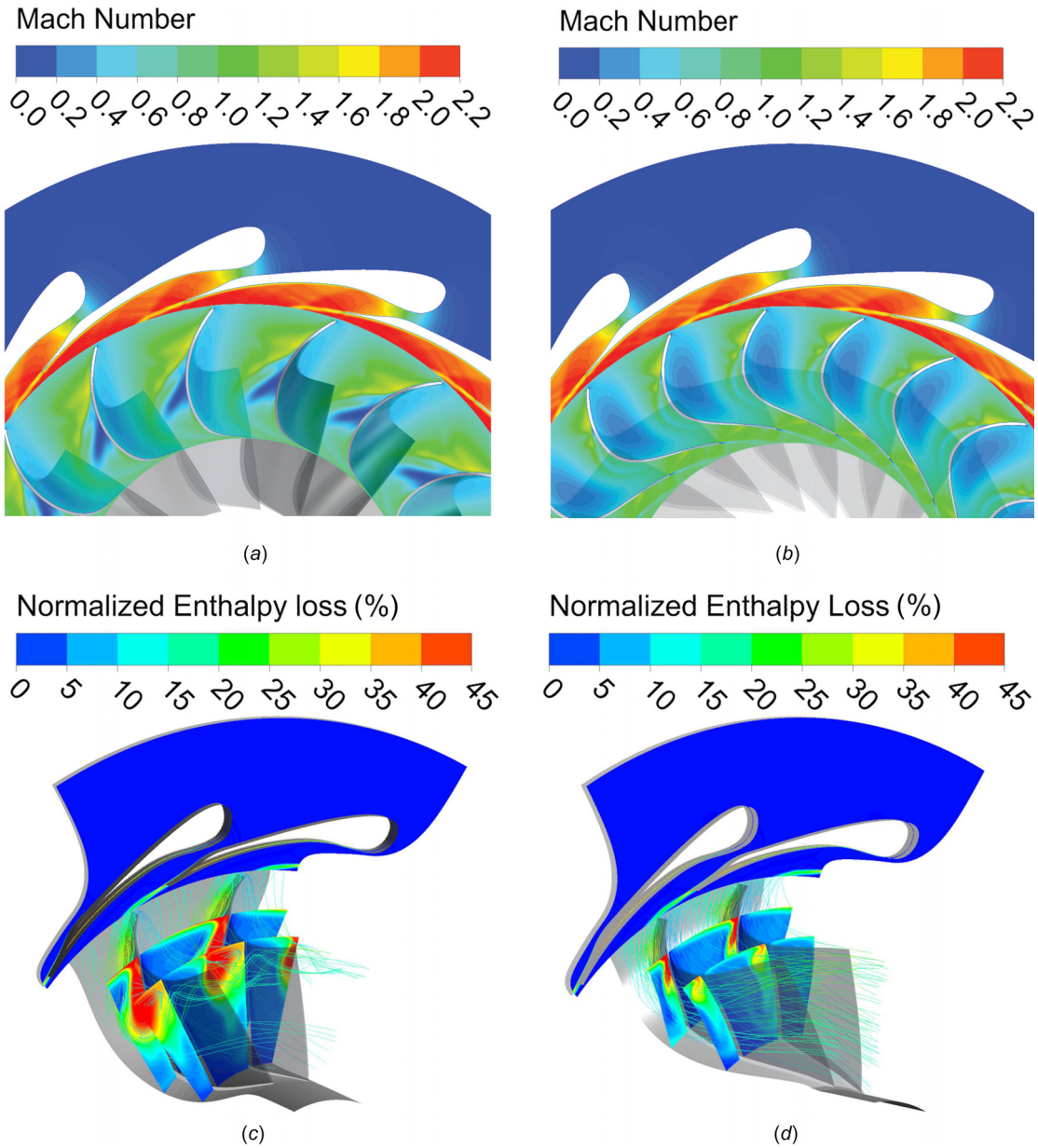

Fig. 6 Flow field Mach number and normalized enthalpy loss ($\Delta h/\Delta h_{ref} \approx T \cdot \Delta s/\Delta h_{ref}$) evaluated at blade midspan. (*a*) and (*c*): baseline geometry; (*b*) and (*d*): optimized geometry.

Table 6 Loss breakdown strategy

Loss type	Averaging procedure	CFD model
Blade profile losses	Midspan: inlet boundary to TE	Free slip endwalls, no tip clearance gap
Mixing loss	Midspan: TE to outlet boundary	Free slip endwalls, no tip clearance gap
Endwall and secondary flow	Spanwise average: inlet to outlet	No tip clearance gap
Tip leakage	Spanwise average: inlet to outlet	Tip clearance gap
Leaving loss	Spanwise average: outlet	Tip clearance gap

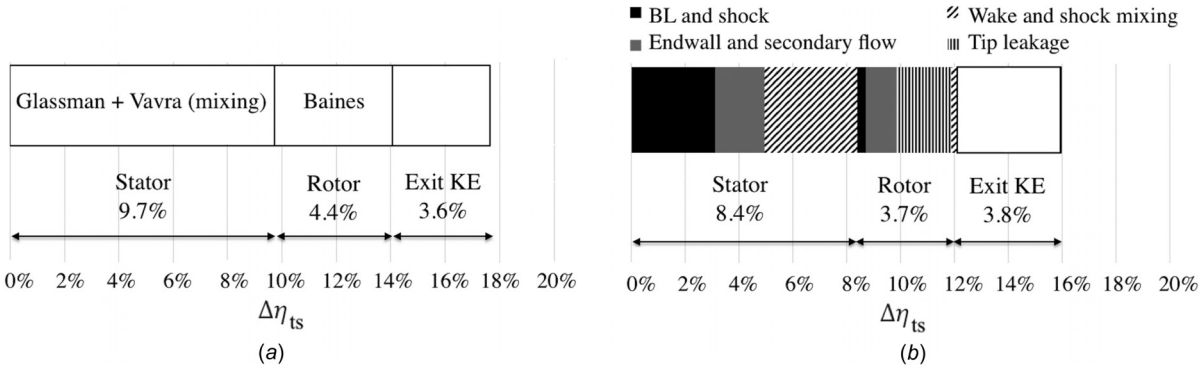

Fig. 7 Loss breakdown: (*a*) meanline results for the optimized geometry and (*b*) CFD results for the optimized geometry

Table 7 Optimized turbine: CFD loss breakdown

	Boundary layer (%)	Wake-shock mixing (%)	Endwall-secondary flow (%)	Tip leakage	Kinetic energy	Total (%)
Stator	3.1	3.4	1.9	—	—	8.4
Rotor	0.3	0.2	1.2	2.0%	3.8%	7.5

3 Loss Breakdown

The flow through the channels of mini-ORC radial-inflow turbines is rather different from that of more conventional turbomachinery; thus, investigating the various types of losses and their distribution can contribute to the extension of design expertise. The entropy generation mechanisms considered in the study are, (i) blade profile losses, i.e., viscous dissipation in boundary layers and dissipation across shock waves on the blade surfaces; (ii) mixing losses, i.e., mixing-out of the trailing-edge (TE) wake, boundary layers, and shock waves downstream of the cascade; (iii) endwall and secondary flow losses, i.e., viscous dissipation on the endwalls and mixing enhancement due to secondary flow; (iv) tip-leakage, i.e., mixing-out of the tip leakage flow within the core flow; (v) leaving loss, i.e., dissipated kinetic energy at rotor outlet. The various loss contributions have been calculated by using the model and the flow quantity averaging procedure as reported in Table 6. The losses of the groups (i) and (ii) have been determined by performing three-dimensional CFD calculations with free slip endwalls and by averaging the flow quantities at midspan in three different locations, namely at the inlet, immediately downstream the TE, and at the outflow boundary. The shock losses are not separately assessed through inviscid calculations, as the blockage caused by boundary layers can affect the shock location and strength. Moreover, the attribution of the entropy generated by shock wave—boundary layer interaction to either boundary layer or shock waves dissipation may be performed only on an arbitrary basis.

Figure 7(*b*) shows the obtained results, expressed as a deficit in total-to-static efficiency. The fluid-dynamic losses in the stator are significantly larger than those in the rotor, confirming the results reported in Ref. [9] for a medium power capacity ORC radial-inflow turbine. More in detail, the major loss contribution in the stator is due to the wake mixing downstream of the vane TE, while the fluid dynamic penalty in the rotor is mainly due to endwalls dissipation, secondary flow-induced mixing and tip-leakage flow. Tip-leakage accounts for more than half of the total losses of the rotor, suggesting the importance of properly sealing the blade tip gap in mini-ORC turbines, see Table 7. Viscous dissipation along the walls is responsible for at least 40% of the total-to-static efficiency deficit; therefore, the accurate modeling of the flow characteristics within boundary layers, especially in nonideal flow conditions, is of paramount importance for reliable efficiency predictions.

In the case of the baseline turbine geometry the impeller losses were found to be higher than those in the stator: the impeller is responsible for a total efficiency deficit of 10.3% compared to 8.1% of the stator. This is the result of higher profile, endwall, and leaving losses. In terms of efficiency debit, leaving losses amount to 5.3% against the 3.8% reported in Table 7 for the optimized geometry.

The results of the CFD simulation are furthermore compared to the results provided by the meanline model, in which the number of blades is assumed equal to the optimal value found through CFD optimization. From the comparison, shown in Fig. 7(*a*), it can be inferred that the use of the loss model by Baines and Glassman, complemented by a physical loss model accounting for shock wave and mixing losses, leads to the underestimation of the overall turbine efficiency value. However, the level of accuracy of these models seems adequate for conceptual design purposes, since the meanline model predicts the loss distribution over the stator and the rotor sufficiently well.

4 Assessment of Stator–Rotor Interaction Effects

The relatively small radial distance between stator and rotor and the high Mach number of the flow at the stator outlet suggest

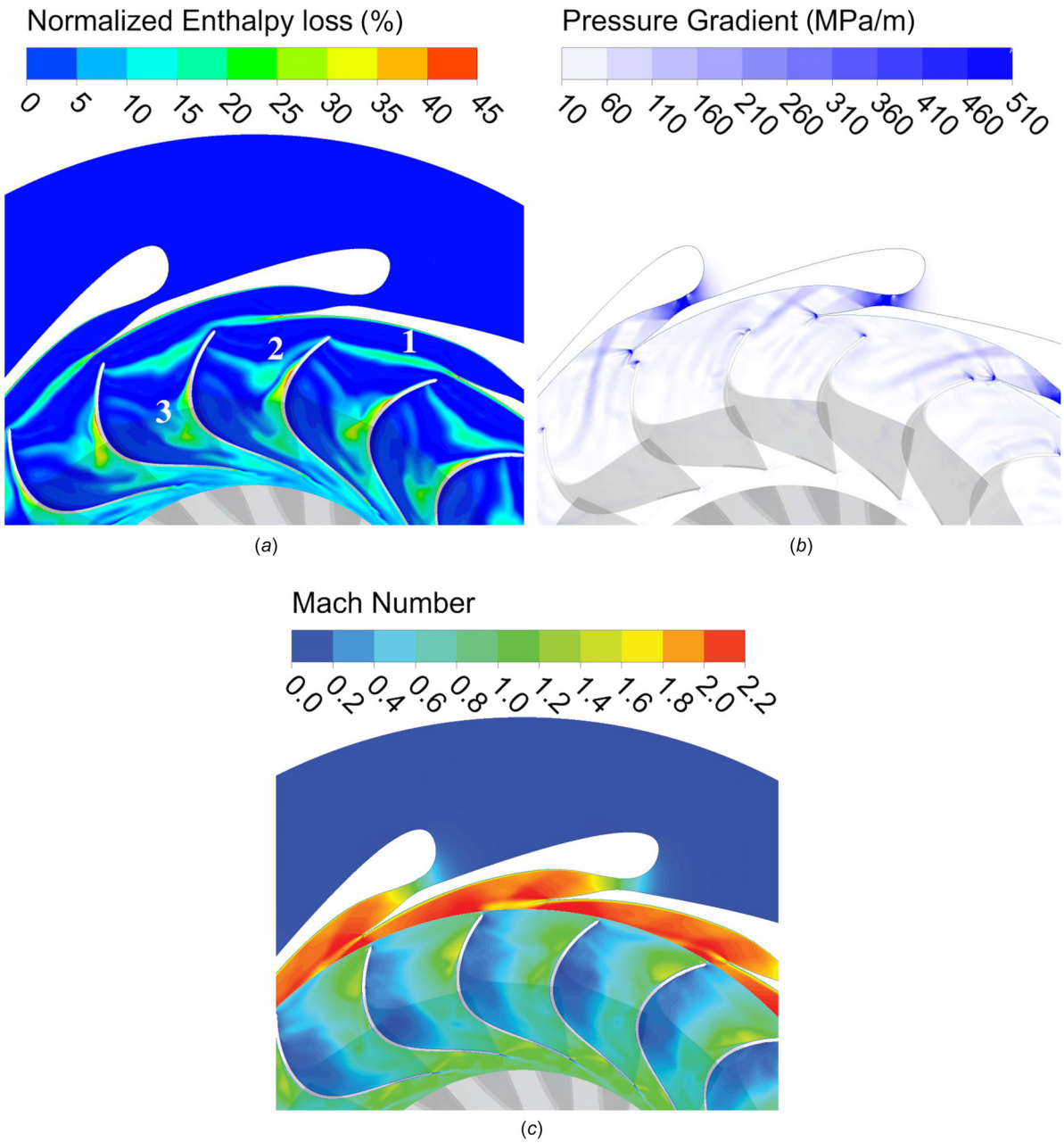

Fig. 8 Snapshot of the unsteady flow field at midspan: (*a*) normalized enthalpy loss ($\Delta h/\Delta h_{ref} \approx T \cdot \Delta s/\Delta h_{ref}$), (*b*) pressure gradient, and (*c*) Mach number

that unsteady stator–rotor interaction effects may negatively affect the fluid-dynamic performance of this type of turbines. For this reason, unsteady CFD computations are used to quantify the impact of flow unsteadiness on turbine efficiency and on aerodynamic blade loading. The same flow solver used for steady-flow simulations has been adopted in this study [25]. In the investigated turbine, the stator–rotor pitch ratio differs from unity, thus chorochronic periodicity must be adopted, see Refs. [30] and [31], in order to simulate only one single stator and rotor flow passage. The solution of the unsteady set of equations was marched in time using a dual time stepping technique and the single rotor passage was reconstructed using 152 physical time steps, corresponding to ~0.2 deg of rotation per time-step.

Unsteady effects at the stator-rotor interface in supersonic ORC turbines are due to potential interaction and wake or shock wave impingement on the rotor pressure surface. Figure 8(*a*) highlights the interaction between the rotor and stator wake. The wake forming at the stator TE remains practically unmixed with the bulk flow for about a rotor pitch, see 1 in Fig. 8(*a*). The wake is then chopped by the rotor leading edge blade, see 2 in Fig. 8(*a*), and transported by the pitchwise pressure gradient toward the rotor suction side. It is finally released at the rotor outlet section, where it mixes with the rest of the flow, see 3 in Fig. 8(*a*). Useful information on stator–rotor interaction caused by shock-waves can be retrieved by visualizing the pressure gradient magnitude. Figure 8(*b*) shows a snapshot of this flow quantity for a full rotor passage. Differently from what is reported in Ref. [32] for a larger radial inflow ORC turbine, the shocks generated by the supersonic stator have a weak effect on the rotor flow-field and do not induce flow separation on the blade suction side, as displayed in Fig. 8(*c*). This result suggests that shock-wave unsteady effects in mini-ORC RITs can be effectively mitigated at nominal operating conditions by designing for subsonic flow at rotor inlet.

The unsteady simulations are also compared with the results obtained with the steady-state flow model. The time-averaged value of the pressure distribution along the stator blade and its

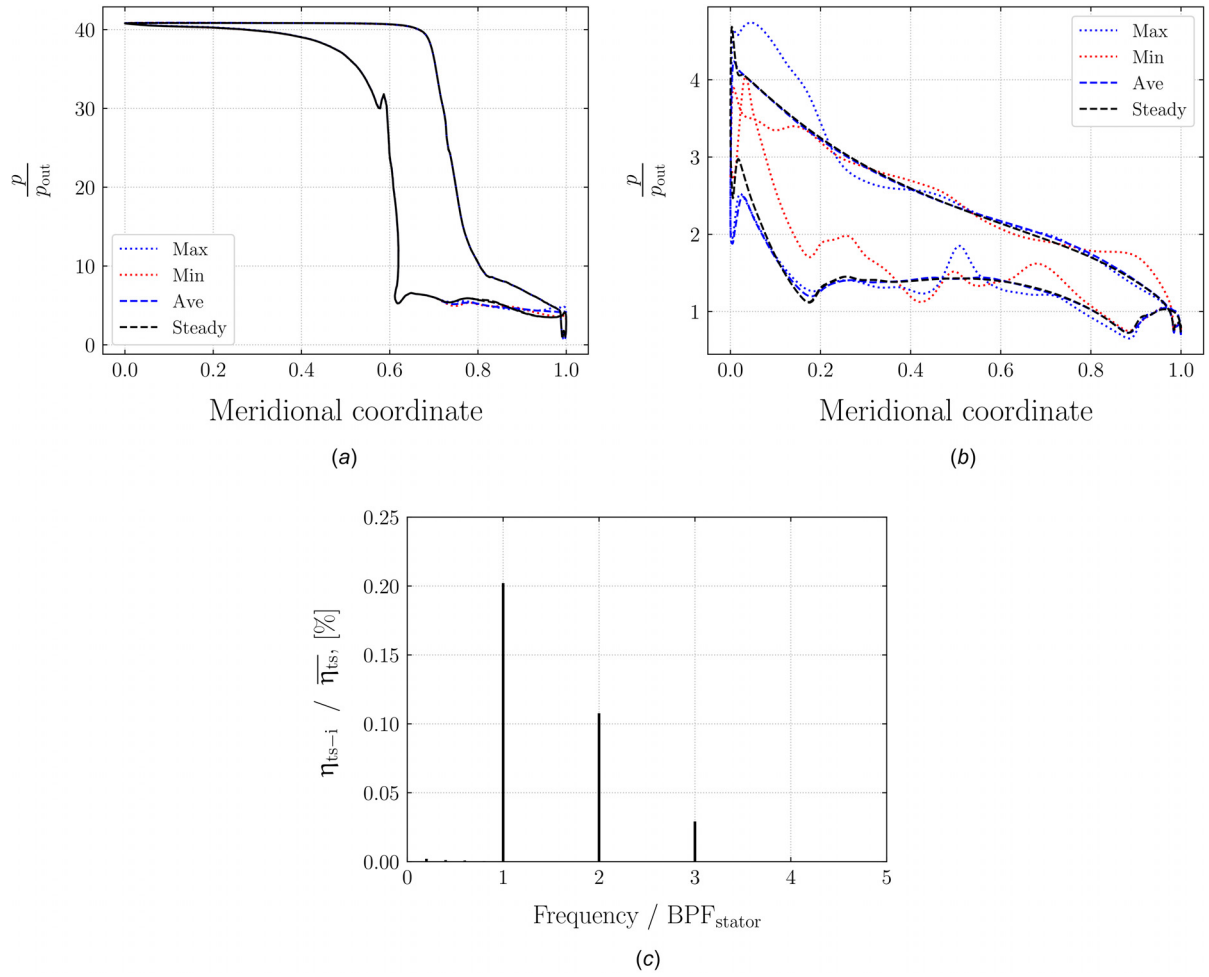

Fig. 9 Unsteady CFD results: (*a*) stator blade loading, (*b*) rotor blade loading, and (*c*) normalized efficiency spectrum

Table 8 Unsteady and steady-state results: relative difference in turbine efficiency, Mach numbers, aerodynamic forces and mass flow rate

$\Delta\eta_{ts}$	ΔM_1	ΔM_{rel-2}	$\Delta F_{t-stator}$	$\Delta F_{t-rotor}$	$\Delta\dot{m}$
0.2%	−0.2%	+4.7%	−0.4%	+2.9%	0.0%

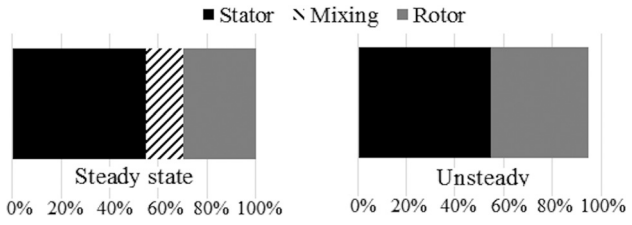

Fig. 10 Unsteady and steady-state results: normalized component losses

minimum and maximum excursions are very close to the aerodynamic loading of the steady calculation, see Fig. 9(*a*). As expected, the aerodynamic loading on the rotor undergoes larger variations, mainly located in the first 30% of the meridional length. The fluctuations are associated with the interaction between the stator wake and the rotor leading edge, which induces pressure oscillations that can be as high as ±11% with respect to time-averaged rotor blade loading, see Fig. 9(*b*). Despite flow unsteadiness seems to play a role with respect to the evaluation of the rotor fluid-dynamic performance, the time-averaged aerodynamic loading is close to the pressure distribution found through steady calculations, indicating that time-averaged and steady turbine efficiency values are in good agreement. This is confirmed by the result displayed in Fig. 9(*c*), which shows the frequency spectrum of the turbine total-to-static efficiency, normalized with respect to the zeroth-order harmonic, i.e., the time-averaged efficiency value. The analysis of the spectrum indicates that higher-order harmonics have minor if no impact on turbine total-to-static efficiency. It can then be argued that steady CFD calculations are suited to assess the averaged fluid-dynamic performance of the mini-ORC RIT under investigation. Table 8 summarizes the normalized deviation of the global quantities of interest between steady and unsteady calculations. The largest deviation is found in the value of the inlet relative rotor Mach number, which reflects the additional fluid-dynamic losses fictitiously introduced upstream of the impeller by the mixing-plane as compared to the unsteady interface, see Fig. 10.

5 Assessment of Part-Load Performance

Despite the small size of the turbine, the results of the fluid dynamic study predict that high efficiency in nominal operating conditions can be obtained if the expander is properly designed. This may not be the case at part loads, due to the high ratio between the inlet and outlet flow passage area of the rotor, and the possible high sensitivity of the supersonic nozzle operation to variations of the pressure ratio. In applications like waste heat recovery from propulsion engines or small-scale concentrated solar

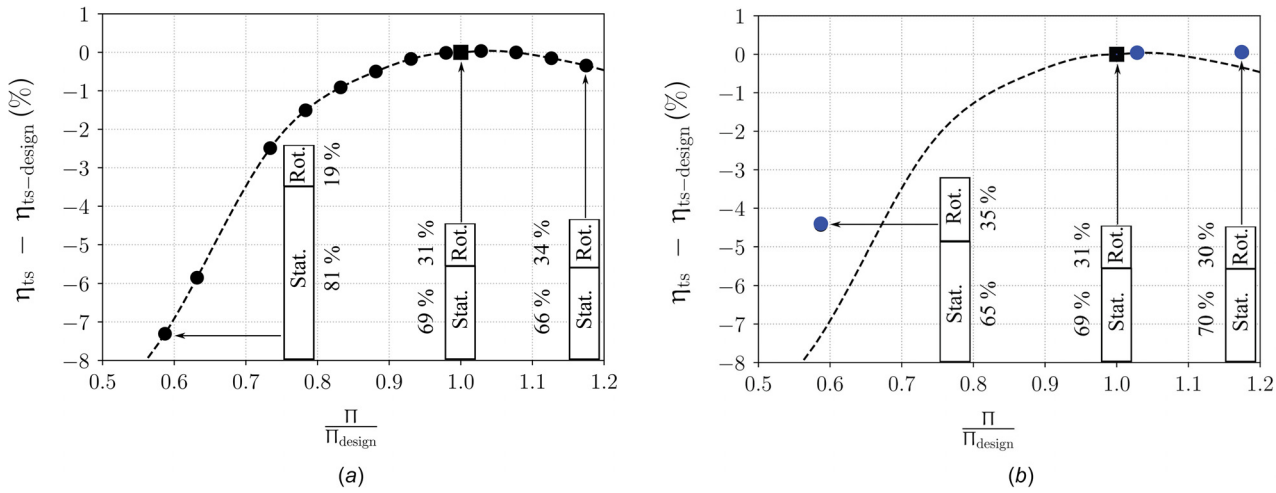

Fig. 11 Part load operation. Total-to-static efficiency as a function of the expansion ratio. The histograms represent the normalized enthalpy loss and the components loss distribution: (*a*) 1 degree-of-freedom: inlet pressure; (*b*) 2 degrees-of-freedom: inlet pressure and rotational speed. The square indicates the turbine on-design conditions.

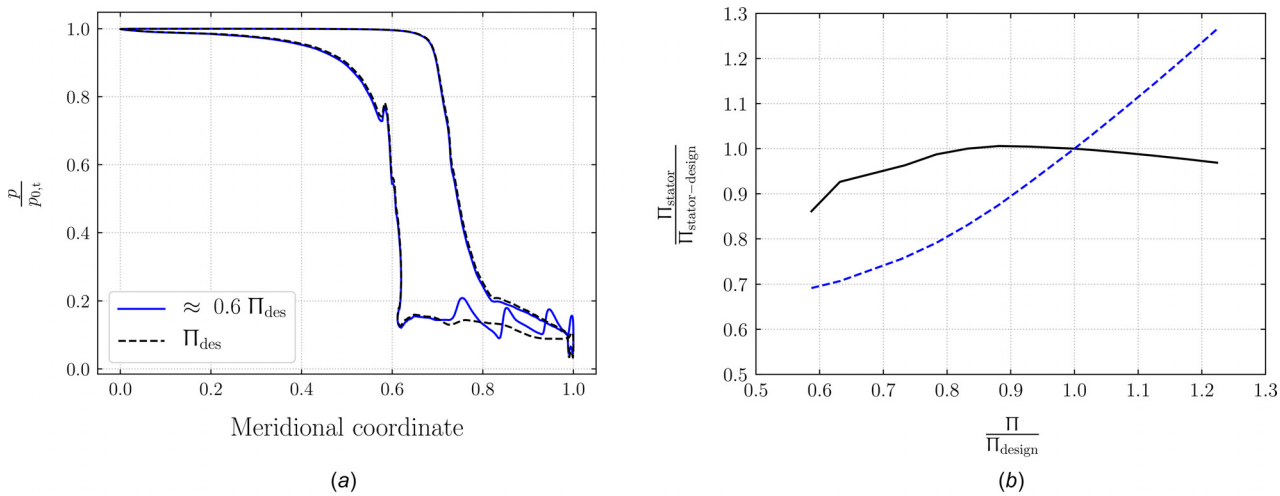

Fig. 12 Normalized pressure distribution along the stator blade for nominal and part load conditions: (*a*) pressure distribution in off-design conditions ($\Pi = 0.6 \cdot \Pi_{design}$, $\omega = \omega_{design}$) and (*b*) expansion ratio of the stator (——) and the rotor (- - - -) at off-design (1 degree-of-freedom: inlet pressure)

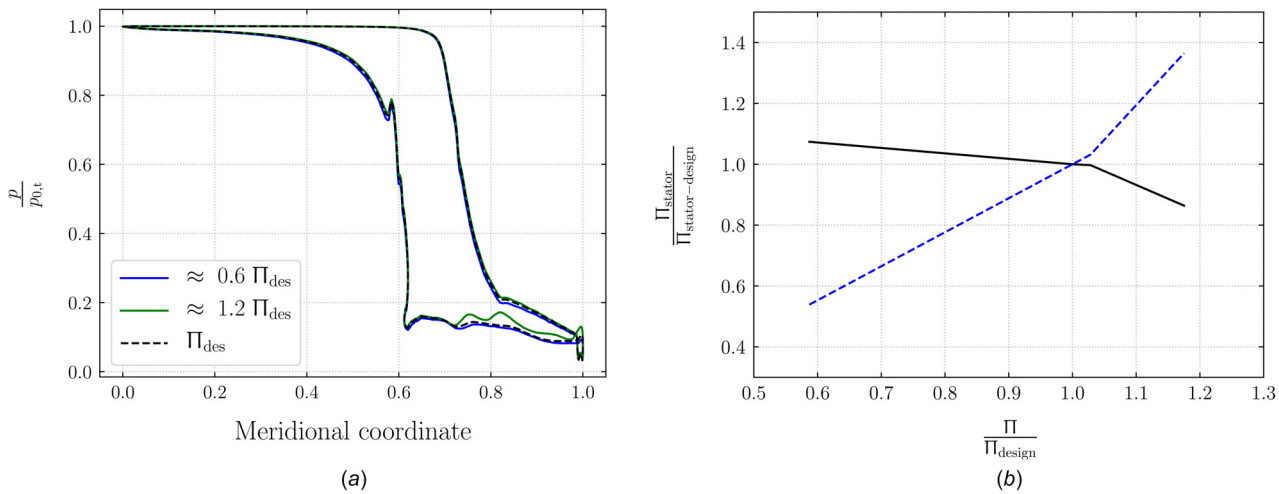

Fig. 13 Normalized pressure distribution along the stator blade for nominal and part load conditions: (*a*) pressure distribution at off-design ($\Pi = 0.6 \cdot \Pi_{design}$, $\omega = 0.88 \cdot \omega_{design}$) and (*b*) expansion ratio of the stator (——) and the rotor (- - - -) in off-design conditions (2 degrees-of-freedom: inlet pressure and ω)

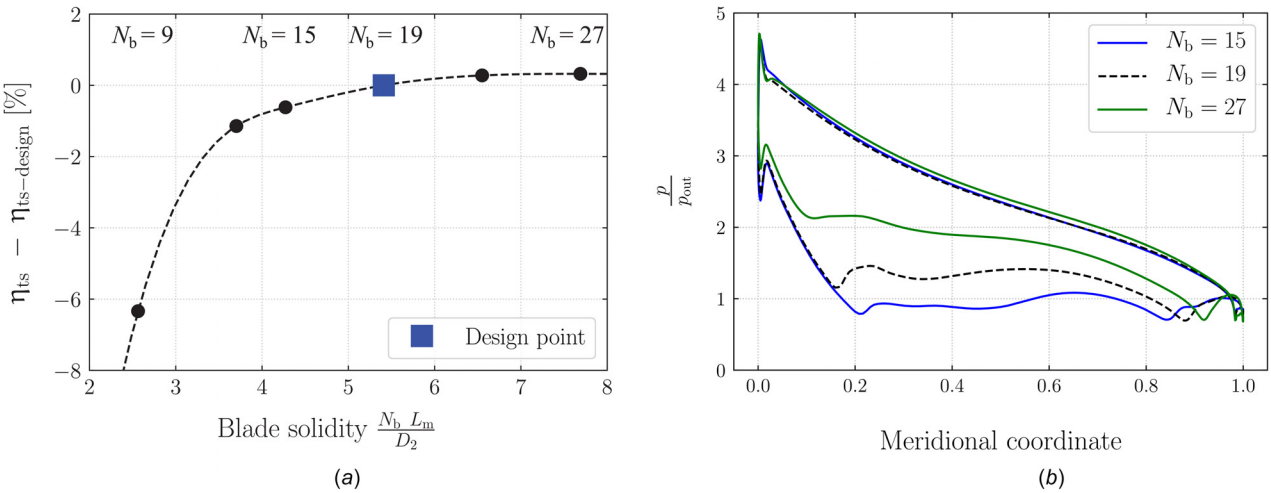

Fig. 14 Influence of rotor solidity: (*a*) efficiency predicted by CFD simulations and (*b*) blade loading

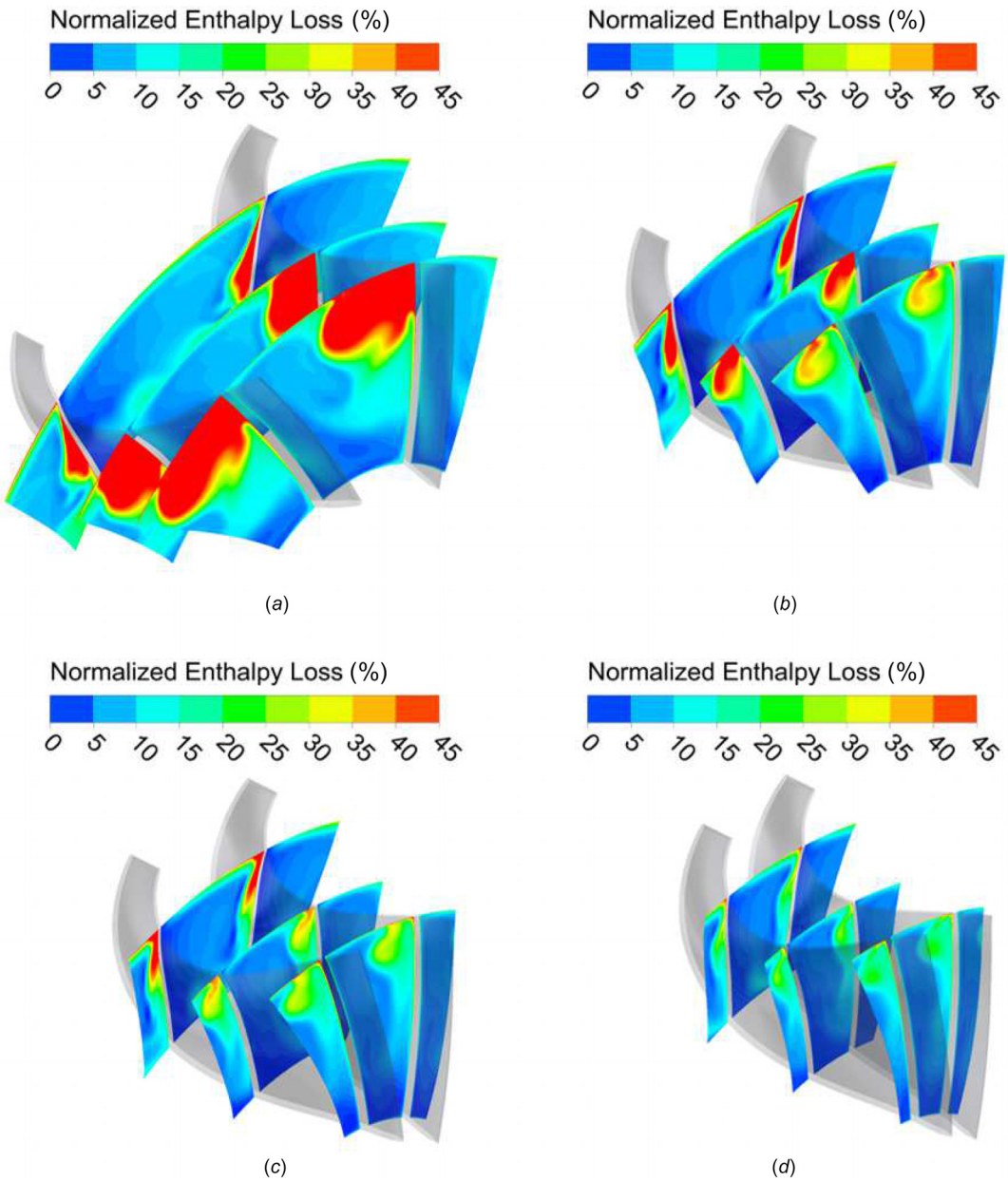

Fig. 15 Normalized enthalpy loss ($\Delta h/\Delta h_{ref} \approx T \cdot \Delta s/\Delta h_{ref}$) in the rotor for different blade numbers: (*a*) $N_b = 9$, (*b*) $N_b = 15$, (*c*) $N_b = 19$, and (*d*) $N_b = 27$

power plants, off-design performance is of great importance. For this reason, an additional study on the steady-state part-load performance of the mini-ORC turbine has been carried out by means of CFD simulations. The results of the study are summarized in Fig. 11. The characteristic curve in Fig. 11(*a*) shows the variation of the total-to-static efficiency as a function of the expansion ratio. The curve has been calculated by keeping the rotational speed constant while varying the inlet total pressure from about 60% to 120% of its nominal value. This range corresponds to a variation between 50% and 125% of the shaft power with respect to the design conditions. The efficiency decay is limited at higher pressure ratios, while it sharply increases as the inlet pressure declines. This is due to the stronger fluid-dynamic penalty in the stator caused by the larger profile losses occurring from the throat to the outlet section. The additional penalty is generated by a series of shock waves forming on the rear suction side as a result of the reduced expansion ratio, which can be recognized in the sharp fluctuations in the pressure distribution of Fig. 12.

The efficiency decay can be mitigated by adjusting the rotational speed of the impeller, as shown in Fig. 11(*b*). In particular, a reduction of ω of 12% is found to provide the best performance for the case with the pressure ratio equal to 60% of the nominal value. In this condition, the efficiency improves thanks to the lower fluid-dynamic losses in the stator, which, however, remain larger than those in the rotor. With respect to the previous case at the nominal speed, the stator operates with a higher expansion ratio, even larger than that at the design point, which allows for an almost shock-free post-expansion, as demonstrated by the smoother pressure distribution on the final part of the nozzle blade in Fig. 13. The gain obtained in the stator efficiency comes at the expense of an increase of the losses in the rotor wheel due to flow separation on the suction surface, which is triggered by a high incidence angle.

6 Assessment of the Optimal Solidity of the Impeller

One of the most important steps in turbomachinery design is the selection of blade solidity. Axial turbines performance is particularly sensitive to variations of this parameter, while for radial impellers the effect of solidity seems to be less critical [3]. Targeted CFD simulations were used to investigate if this observation applies also to ORC radial inflow rotors characterized by large volumetric flow ratios.

Figure 14(*a*) depicts the change in turbine efficiency as a function of the number of rotor blades. Apart from relatively low blade numbers which lead to flow separation on the blade suction side, see Fig. 15, the fluid-dynamic performance is found to be almost independent from the solidity parameter, notwithstanding its large influence on blade loading, see Fig. 14(*b*). A sort of plateau in the total-to-static efficiency is predicted for blade numbers in the range of 15–27, which are the values suggested by the Glassman and Jamieson correlations, respectively. The Whitfield model provides an intermediate value of 19, which coincides with the one selected for the final turbine design presented in Sec. 2.2.2. The trend displayed in Fig. 14(*a*) is in line with the experimental findings of Rodgers [3] for radial gas turbines, who showed that the efficiency value for optimally designed turbines is weakly dependent on the blade counts, if the blade solidity is above 4.0.

From this outcome, it can be argued that all the available correlations for blade number estimation can be adopted to determine the solidity of radial ORC turbines, although these models yield substantially different results. The optimal value can then be chosen according to manufacturing criteria rather than fluid-dynamic considerations.

7 Conclusions

The detailed design and the numerical investigation of the fluid dynamic performance of a mini-ORC radial inflow turbine have been documented in this paper. Notwithstanding the small turbine dimensions, the nominal total-to-static efficiency of the turbine was predicted by both steady and unsteady CFD calculations to be about 84%, in the case tip gap is considered. This estimate indicates that supersonic mini-ORC turbines elaborating expansion ratios of the order of 50 can be designed to achieve relatively high fluid-dynamic performance, provided that specialized methods are used to shape the stator and rotor blade profiles. The reason thereof is arguably that the use of a highly complex working fluid, which exhibits comparatively low enthalpy drops, allows to design these machines for load and flow coefficients close to the optimal values for radial turbines, while attaining low dissipation across shock waves as compared to simpler fluid molecules.

Based on the results of this study, and pending experimental verification, the following conclusions regarding radial-inflow mini-ORC turbines can be drawn:

(1) As opposed to conventional radial-inflow machines, the stator is affected from higher fluid-dynamic losses. Most of the entropy generation is due to viscous dissipation in the boundary layers and mixing downstream of the cascade.
(2) The rotor fluid-dynamic penalty is mainly caused by secondary flows and tip-leakage flows.
(3) Comparison between unsteady and steady CFD calculations revealed that time-averaged turbine efficiency and aerodynamic forcing are well in agreement with the values predicted by the steady-state model. Moreover, the maximum and minimum values of the corresponding time-varying envelope differ by few percents. Stator–rotor interaction effects seem thus to be of minor relevance for the fluid-dynamic design of these turbines.
(4) The turbine off-design performance decays appreciably for load values below 80% of the nominal value, due to the increasing fluid-dynamic losses in the stator as the pressure ratio reduces. These penalties can be effectively mitigated by adjusting the rotational speed.
(5) Existing correlations for the selection of rotor blade number, originally developed for turbochargers and gas turbines, are also applicable to high-volumetric-flow-ratio mini-ORC turbines, since the efficiency of these machines shows weak dependence from solidity.

Although the outlined conclusions still demand for the planned experimental validation, the results of this study can be considered a first necessary step toward the definition of new design practices applicable to mini-ORC turbines.

Acknowledgment

This research has been supported by Bosch GmbH and the Applied and Engineering Sciences Domain (TTW) of the Dutch Organization for Scientific Research (NWO), Technology Program of the Ministry of Economic Affairs, Grant No. 13385.

Funding Data

- Technology Program of the Ministry of Economic Affairs (Grant No. 13385; Funder ID: 10.13039/501100004725).

Supplemental Data

The turbine geometry can be downloaded at the website link.[2]

Nomenclature

Symbols

a = width of the blade channel at the outlet section (mm)
D = diameter (mm)

[2]https://bitbucket.org/pp-team/orchidturbine/downloads/

D_s = specific diameter
F = force (N)
h = enthalpy (kJ/kg)
L_m = length of the mean meridional flow path (mm)
M = Mach number
$\dot{m}$ = mass flow rate (kg/s)
N_b = number of blades
N_s = specific speed
p = pressure (kPa)
r = radius (mm)
R = reaction degree
s = entropy (kJ/kg K), blade pitch (mm)
t = thickness (mm)
T = temperature (K)
U = peripheral speed (m/s)
V = absolute velocity (m/s)
VR = volumetric ratio
$\dot{W}$ = power (kW)
y^+ = dimensionless wall distance

Greek Symbols

α = absolute flow angle (deg)
β = relative flow angle, blade metal angle (deg)
ϵ = rotor tip gap (mm)
η = efficiency
Π = expansion ratio
ρ = density (kg/m^3)
ϕ = flow coefficient
ψ = load coefficient
ω = rotational speed (krpm)

Subscripts

a = blade channel outlet section
is = isentropic
m = meridional
nom = nominal condition
r = radial direction
rel = relative velocity
ref = reference condition
rot = rotor
t = total
te = trailing edge
ts = total to static
tt = total to total
x = axial direction
0 = stator inlet
1 = stator outlet
2 = rotor inlet
3 = rotor outlet

References

[1] Colonna, P., Casati, E., Trapp, C., Mathijssen, T., Larjola, J., Turunen-Saaresti, T., and Uusitalo, A., 2015, "Organic Rankine Cycle Power Systems: From the Concept to Current Technology, Applications, and an Outlook to the Future," ASME J. Eng. Gas Turbines Power, **137**(10), p. 100801.
[2] Colonna, P., Nannan, N., Guardone, A., and Lemmon, E. W., 2006, "Multiparameter Equations of State for Selected Siloxanes," Fluid Phase Equilib., **244**(2), pp. 193–211.
[3] Rodgers, C., 1987, *High Pressure Ratio Turbine Design Constraints* (Lecture Series on Small High Pressure Ratio Turbines, Vol. 7), Von Karman Institute for Fluid Dynamics, Rhode Saint Genèse, Belgium.
[4] Meitner, P. L., and Glassman, A. J., 1983, "Computer Code for Off-Design Performance Analysis of Radial-Inflow Turbines With Rotor Blade Sweep," NASA Lewis Research Center, Cleveland, OH, Report No. TP-2199.
[5] Whitfield, A., 1990, "The Preliminary Design of Radial Inflow Turbines," ASME J. Turbomach., **112**(1), pp. 50–57.
[6] Demierre, J., Rubino, A., and Schiffmann, J., 2014, "Modeling and Experimental Investigation of an Oil-Free Microcompressor-Turbine Unit for an Organic Rankine Cycle Driven Heat Pump," ASME J. Eng. Gas Turbines Power, **137**(3), p. 032602.
[7] Sauret, E., 2012, "Open Design of High Pressure Ratio Radial-Inflow Turbine for Academic Validation," ASME Paper No. IMECE2012-88315.
[8] Fiaschi, D., Innocenti, G., Manfrida, G., and Maraschiello, F., 2016, "Design of Micro Radial Turboexpanders for ORC Power Cycles: From 0D to 3D," J. Appl. Therm. Eng., **99**, pp. 402–410.
[9] Wheeler, A., and Ong, J., 2014, "A Study of the Three-Dimensional Unsteady Real-Gas Flows Within a Transonic ORC Turbine," ASME Paper No. GT2014-25475.
[10] Anand, N., Vitale, S., Pecnik, R., Otero, G., and Pini, M., 2018, "Design Methodology for Supersonic Radial Vanes Operating in Non-Ideal Flow Conditions," ASME J. Eng. Gas Turbines Power, **141**(2), p. 022601.
[11] White, M. T., Markides, C. N., and Sayma, A. I., 2018, "Working-Fluid Replacement in Supersonic Organic Rankine Cycle Turbines," ASME J. Eng. Gas Turbines Power, **140**(9), p. 091703.
[12] Costall, A. W., Hernandez, A. G., Newton, P. J., and Martinez-Botas, R., 2015, "Design Methodology for Radial Turbo Expanders in Mobile Organic Rankine Cycle Applications," J. Appl. Energy, **157**, pp. 729–743.
[13] Head, A. J., De Servi, C., Casati, E., Pini, M., and Colonna, P., 2016, "Preliminary Design of the ORCHID: A Facility for Studying Non-Ideal Compressible Fluid Dynamics and Testing Orc Expanders," ASME Paper No. GT2016-56103.
[14] Pini, M., De Servi, C., Burigana, M., Bahamonde, S., Rubino, A., Vitale, S., and Colonna, P., 2017, "Fluid-Dynamic Design and Characterization of a Mini-Orc Turbine for Laboratory Experiments," Energy Procedia, **129**, pp. 1141–1148.
[15] Macchi, E., and Perdichizzi, A., 1981, "Efficiency Prediction for Axial-Flow Turbines Operating With Nonconventional Fluids," ASME J. Eng. Power, **103**(4), pp. 718–724.
[16] Da Lio, L., Manente, G., and Lazzaretto, A., 2016, "Predicting the Optimum Design of Single Stage Axial Expanders in Orc Systems: Is There a Single Efficiency Map for Different Working Fluids?," Appl. Energy, **167**, pp. 44–58.
[17] Da Lio, L., Manente, G., and Lazzaretto, A., 2017, "A Mean-Line Model to Predict the Design Efficiency of Radial Inflow Turbines in Organic Rankine Cycle (Orc) Systems," Appl. Energy, **205**, pp. 187–209.
[18] Bahamonde, S., Pini, M., De Servi, C., Rubino, A., and Colonna, P., 2017, "Method for the Preliminary Fluid Dynamic Design of High-Temperature Mini-Orc Turbines," ASME J. Eng. Gas Turbine Power, **139**(8), p. 082606.
[19] Dreizler, M., 2015, "Bosch Corporate Research GmbH, Internal Report," Personal Communication.
[20] Qiu, X., and Baines, N., 2007, "Performance Prediction for High Pressure-Ratio Radial Inflow Turbines," ASME Paper No. GT2007-27057.
[21] Vavra, M. H., 1960, *Aero-Thermodynamics and Flow in Turbomachines*, Wiley, New York.
[22] Pini, M., Persico, G., Pasquale, D., and Rebay, S., 2014, "Adjoint Method for Shape Optimization in Real-Gas Flow Applications," ASME J. Eng. Gas Turbines Power, **137**(3), p. 032604.
[23] Deych, M. Y., and Troyanovskiy, B., 1964, "Investigation and Calculation of Axial Turbine Stages," U.S. Air Force, Foreign Technology DIV., Wright-Patterson Air Force Base, OH, Document No. FTD-MT-65-409.
[24] Glassman, A., 1976, "Computer Program for Design Analysis of Radial-Inflow Turbines," NASA Lewis Research Center, Cleveland, OH, Report No. D-8164.
[25] ANSYS, 2017, "ANSYS® Workbench, Release 17.1," ANSYS, Canonsburg, PA.
[26] Chung, T. H., Ajlan, M., Lee, L. L., and Starling, K. E., 1988, "Generalized Multiparameter Correlation for Nonpolar and Polar Fluid Transport Properties," Ind. Eng. Chem. Res., **27**(4), pp. 671–679.
[27] Colonna, P., van der Stelt, T., and Guardone, A., 2014, "Fluidprop (Version 3.0): A Program for the Estimation of Thermophysical Properties of Fluids," Delft University of Technology, Delft, The Netherlands.
[28] Mueller, L., Alsalihi, Z., and Verstraete, T., 2012, "Multidisciplinary Optimization of a Turbocharger Radial Turbine," ASME J. Turbomach., **135**(2), p. 021022.
[29] Zangeneh-Kazemi, M., Dawes, W., and Hawthorne, W., 1988, "Three Dimensional Flow in Radial-Inflow Turbines," ASME Paper No. 88-GT-103.
[30] He, L., 1990, "An Euler Solution for Unsteady Flows Around Oscillating Blades," ASME J. Turbomach., **112**(4), pp. 714–722.
[31] Gerolymos, G. A., Michon, G. J., and Neubauer, J., 2002, "Analysis and Application of Chorochronic Periodicity in Turbomachinery Rotor/Stator Interaction Computations," J. Propul. Power, **18**(6), pp. 1139–1152.
[32] Rinaldi, E., Pecnik, R., and Colonna, P., 2016, "Unsteady Operation of a Highly Supersonic Organic Rankine Cycle Turbine," ASME J. Turbomach., **138**(12), p. 121010.